J. Fluid Mech. (1994), *vol.* 269, *pp.* 79–106

The flow structure in the lee of an inclined 6:1 prolate spheroid

By T. C. FU[1]†, A. SHEKARRIZ[1]‡, J. KATZ[1] AND T. T. HUANG[2]

[1] Department of Mechanical Engineering, The Johns Hopkins University, Baltimore, MD 21218, USA

[2] David Taylor Model Basin, CD/NSWC, Bethesda, MD 20084-5000, USA

(Received 27 October 1992 and in revised form 10 December 1993)

Particle displacement velocimetry is used to measure the velocity and vorticity distributions around an inclined 6:1 prolate spheroid. The objective is to determine the effects of boundary-layer tripping, incidence angle, and Reynolds number on the flow structure. The vorticity distributions are also used for computing the lateral forces and rolling moments that occur when the flow is asymmetric. The computed forces agree with results of direct measurements. It is shown that when the flow is not tripped, separation causes the formation of a pair of vortex sheets. The size of these sheets increases with increasing incidence angle and axial location. Their orientation and internal vorticity distribution also depend on incidence. Rollup into distinct vortices occurs in some cases, and the primary vortex contains between 20% and 50% of the overall circulation. The entire flow is unsteady and there are considerable variations in the instantaneous vorticity distributions. The remainder of the lee side, excluding these vortex sheets, remains almost vorticity free, providing clear evidence that the flow can be characterized as open separation. Boundary-layer tripping causes earlier separation on part of the model, brings the primary vortex closer to the body, and spreads the vorticity over a larger region. The increased variability in the vorticity distribution causes considerable force fluctuations, but the mean loads remain unchanged. Trends with increasing Reynolds number are conflicting, probably because of boundary-layer transition. The separation point moves towards the leeward meridian and the normal force decreases when the Reynolds number is increased from 0.42×10^6 to 1.3×10^6. Further increase in the Reynolds number to 2.1×10^6 and tripping cause an increase in forces and earlier separation.

1. Introduction

The structure of three-dimensional separated flows has baffled researchers for quite some time and is still not clearly understood. Extensive efforts by Wang (1972, 1983), Wang *et al.* (1990), and Peake & Tobak (1982) led to the understanding that two distinct types of flow separation can exist behind inclined bodies of revolution. The first type, typically defined as 'closed separation', involves an *enclosed* region bounded by a stream surface that intersects the body at the separation and reattachment lines. The second type, 'open separation', involves detachment of stream surfaces from a body at the separation line, but without reattachment of these surfaces further downstream. Consequently, the flow field does not necessarily contain an enclosed separated region (bubble) and, except for the detaching stream surface, the flow can remain attached to

† Present address: David Taylor Model Basin, CD/NSWC, Bethesda, MD 20084-5000, USA.

‡ Present address: Battelle, Pacific Northwest Laboratories, Richland, WA 99352, USA.

the body. According to some references (Costis, Hoang & Telionis 1989; and Wang *et al.* 1990, for example) both forms of separation can occur on the same body, depending on the incidence angle.

Considerable attention has focused on inclined prolate spheroids with a variety of length-to-diameter ratios. Unlike the computed results, which provide detailed distributions of the velocity and vorticity (Kim & Patel 1991*a*, *b* and Gee, Cummings & Schiff 1992 are examples), most of the experimental studies are limited to measurements of surface shear stresses (Meier & Kreplin 1980) and surface flow visualization (Han & Patel 1979; Costis *et al.* 1989; Wang *et al.* 1990). Velocity measurements away from the body, such as the data provided by Meier, Kreplin & Vollmers (1983) as well as by Barber & Simpson (1990), are scarce. Both studies were performed with point measurement techniques, the former with a multi-port Pitot tube and the latter with combined hot wires and a Pitot tube for turbulence and mean velocity measurements. Some qualitative flow visualization experiments utilizing laser sheets and dye (Meier *et al.* 1983; Costis *et al.* 1989; Han & Patel 1979) have also been performed. Consequently, the currently available experimental data are insufficient for comparison with the computed results.

Almost all of the available sources claim that changes in the Reynolds number cause considerable changes in the location of separation, a trend mostly attributed to boundary-layer transition (Han & Patel 1979, for example). Secondary vortex structures that can be easily identified at low Reynolds numbers are hard to detect when the flow becomes unsteady, particularly when point measurement techniques are utilized. As a result, Meier *et al.* (1983) had no difficulties in plotting the cross-flow topology at low velocities, but could not decide whether the vortex pair located near the surface disappeared, or the flow became unsteady to the level that they could not identify them. This particular problem can only be solved by mapping the instantaneous velocity distribution, an option made possible by implementing the particle displacement velocimetry (PDV) method. This approach can overcome the smearing of data caused, for example, by the meandering of structures and is also non-intrusive.

Detailed mapping of the flow structure in the lee side of an inclined prolate spheroid is the primary focus of this paper. As the results show, the instantaneous velocity and vorticity distributions enable identification of primary and secondary vortex structures even when the flow is unsteady and turbulent. From these distributions the circulation as well as the lateral forces are estimated. The effect of several parameters, such as the incidence angle, Reynolds number and boundary-layer tripping are investigated.

2. Experimental set-up

The experiments were performed in a 140 ft long and 10×5 ft cross-section towing tank located at the David Taylor Model Basin (DTMB). The test model was a sting-mounted 9 in. diameter (D_{max}), 6:1 prolate spheroid. The 2 in. diameter sting was attached to a vertical strut that was connected to the carriage. Most of the measurements were performed at 10° and 20° incidence, and at carriage velocities (U) ranging between 1 to 5 ft s^{-1} (corresponding to Reynolds numbers, based on the model length, ranging between 0.42×10^6 to 2.1×10^6). A 2 mm diameter wire, cemented to the surface at $x/L = 0.2$ (x is the axial distance from the nose, and L is the length of the model), was used for tripping the boundary layer during some of the experiments.

The velocity distribution was measured using PDV. A schematic description of the experimental set-up is presented in figure 1(*a*, *b*). Detailed information on the optical

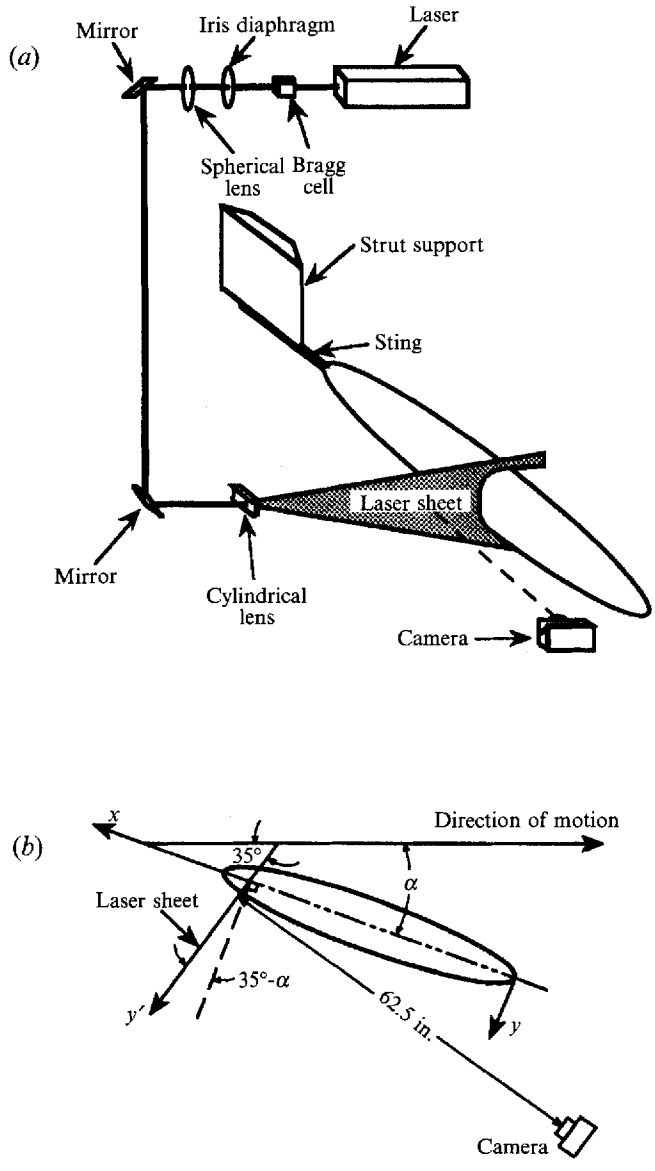

FIGURE 1. A sketch of (*a*) the experimental set-up in the towing tank; (*b*) the orientation of the laser sheet and coordinate system.

set-up is provided by Shekarriz *et al.* (1992*a*, *b*), and the analysis procedures are described by Dong, Chu & Katz (1992*a*, *b*). Most of the images were recorded by a submerged 35 mm camera, primarily since the film met the required resolution (at least 3000×2000 pixels per negative) for PDV. Video images were recorded for qualitative observations, and for determining the location of the separation point. Microscopic (20–30 μm) neutrally buoyant particles containing fluorescent dye were used as tracers. They were distributed in the vicinity of the laser sheet (which was 5 mm thick) prior to each run. Owing to the size of the facility, it was impossible to seed the entire volume. The negatives were digitized by a linear scanner to an array of 3072×2048 pixels (the corresponding real image size was 35×24 cm), and then analysed. The analysis

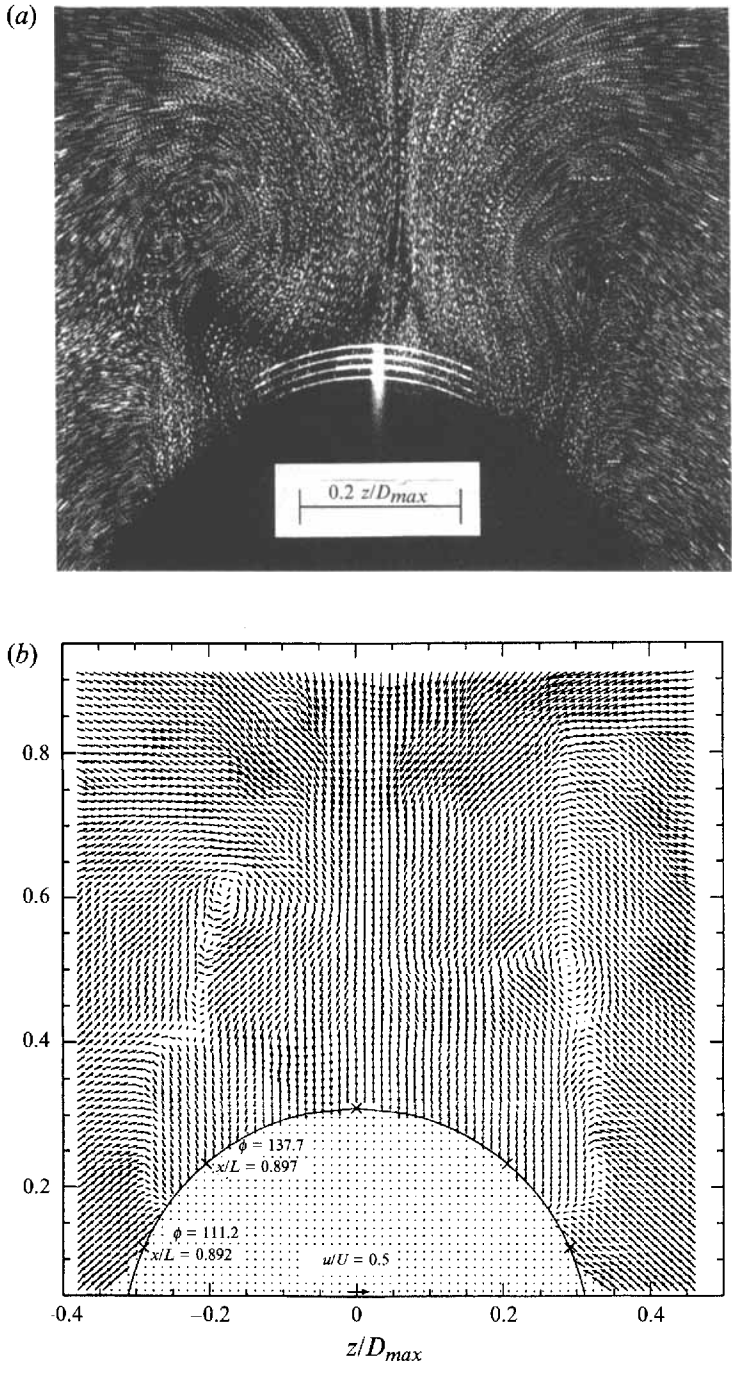

FIGURE 2. (*a*) An image of flow in the lee of an inclined prolate spheroid at $Re_L = 2.1 \times 10^6$, $\alpha = 20°$, and $x/L = 0.90$. (*b*) The instantaneous velocity distribution computed from the image in (*a*). Note that observations are made from the front of the body.

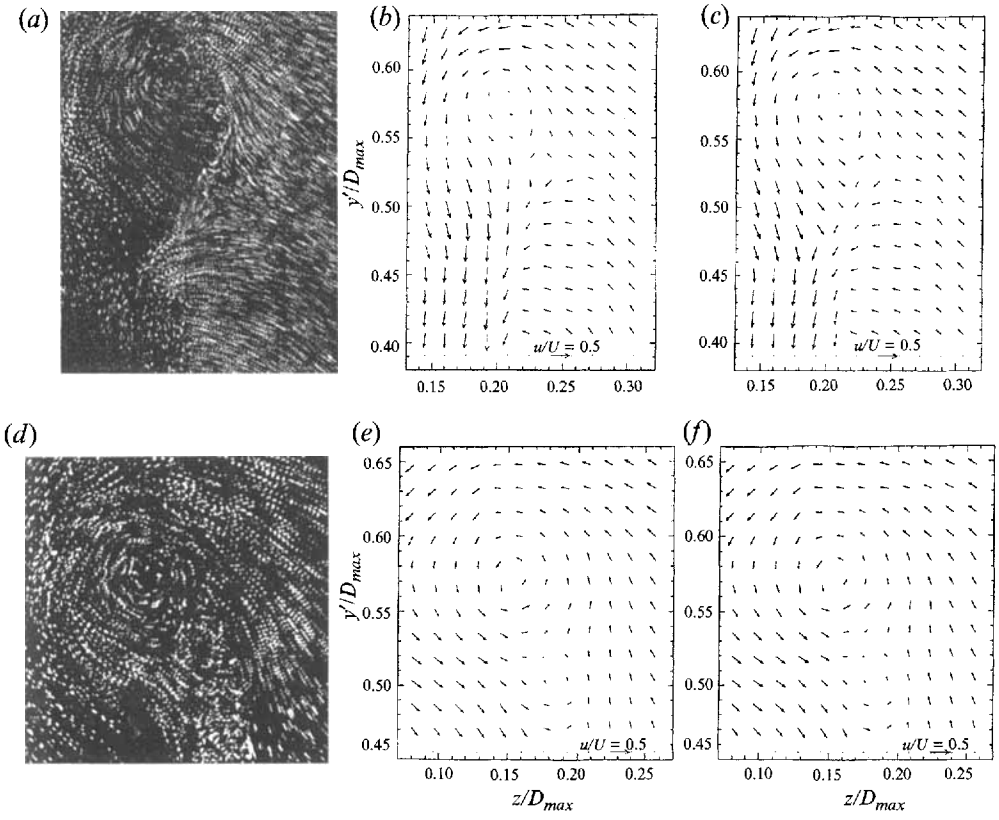

FIGURE 3. Magnified sections focusing on: (*a–c*) a saddle point and the corresponding vector maps; (*d–f*) the primary and secondary structures near a focus and the corresponding vector maps. All are at $x/L = 0.90$, $Re_L = 2.1 \times 10^6$, and $a = 20°$.

procedure consisted of dividing the image into a large number of small sections, and determining the average displacement of all particles within each section by computing the auto-correlation function of the intensity distribution. The size of an interrogation window was 64×64 pixels, corresponding to an area of about 7×7 mm in the flow field. Neighbouring windows were overlapped in part to increase the density of vectors. A typical step was 32 pixels. Calibration experiments (Dong *et al.* 1992*a*) have shown that the error level could be kept at about 1 %, provided several conditions, such as particle density (about 8 particles per window) and resolution (particle diameter ~ 5 pixels) were satisfied. In cases with insufficient seeding, higher magnification could compensate for the lack of tracers. Note that the auto-correlation method computed the average velocity within each window. If the velocity within a certain window varied significantly, the result could be inaccurate owing to broadening of the correlation peaks. Examples of such occurrences, and methods used to solve them will be discussed shortly.

In the present study the laser sheet and the recording equipment were kept at a fixed position. Owing to the geometry of the body, and our desire to measure the velocity near $x/L = 1.0$, it was necessary to position the camera ahead of the model, and to incline the laser sheet at an angle of 35° to the axis of the tank (see figure 1*b*). Consequently, when the model was at 20° incidence, there was a 15° angle between the illuminated plane and the normal to the axis of the model. This arrangement increased

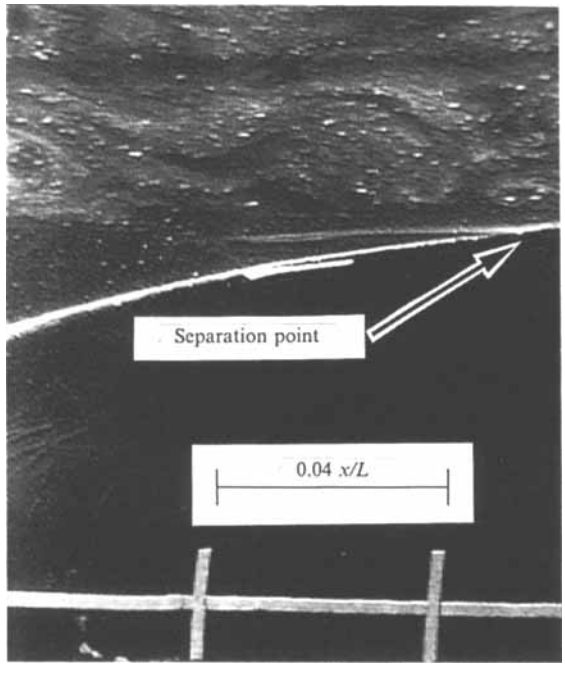

FIGURE 4. An image of an axial sheet containing dye traces used to determine the location of separation.

the residence time of each particle within the light sheet and simplified the recording procedures by enabling us to increase the delay between exposures, which for most of the data presented here was 1 ms. No attempt was made to interpolate or add data to regions with insufficient particle seeding or when the body blocked part of the image.

A sample photograph, recorded by exposing the film four times, and the corresponding velocity vector map are presented in figures 2(*a*) and 2(*b*), respectively. The presence of two 'major' vortex structures (foci) and the saddle points below them are evident. Note that the locations of these singular points depend on the orientation of the laser sheet. In this particular case (20° incidence) there is only a 15° angle between the light sheet and the cross-planes (see figure 1*b*). Thus, there is only about 3.4% difference ($1-\cos 15°$) in the velocities, and the flow structures should be quite similar. Several co-rotating secondary vortices can also be identified below the primary structure to the left side of the model. A similar phenomenon has been identified by Ward & Katz (1989*a*, *b*) during qualitative visualization experiments in the lee side of a nose cone with a sharp tip.

The instantaneous velocity distribution in figure 2(*b*) appears to be asymmetric. Examination of numerous images, some of which will be presented later, leads to the conclusion that this asymmetry is a result of meandering of the vorticity sheet. In other images the primary structure on the right side is higher, and in some they are symmetric. When averaged, the flow structure in the lee of the model appears to be symmetric. Note also that, owing to narrowing of the body, the velocity is not zero even outside the region affected by flow separation.

Figures 3(*a*) and 3(*d*) are close-up views of specific sections in order to provide clearer details of characteristic flow structures on the lee side. The first image shows the flow in the vicinity of a saddle point, and the second provides clear evidence for the existence of 'secondary' vortices below the primary structure. The distinction between 'primary'

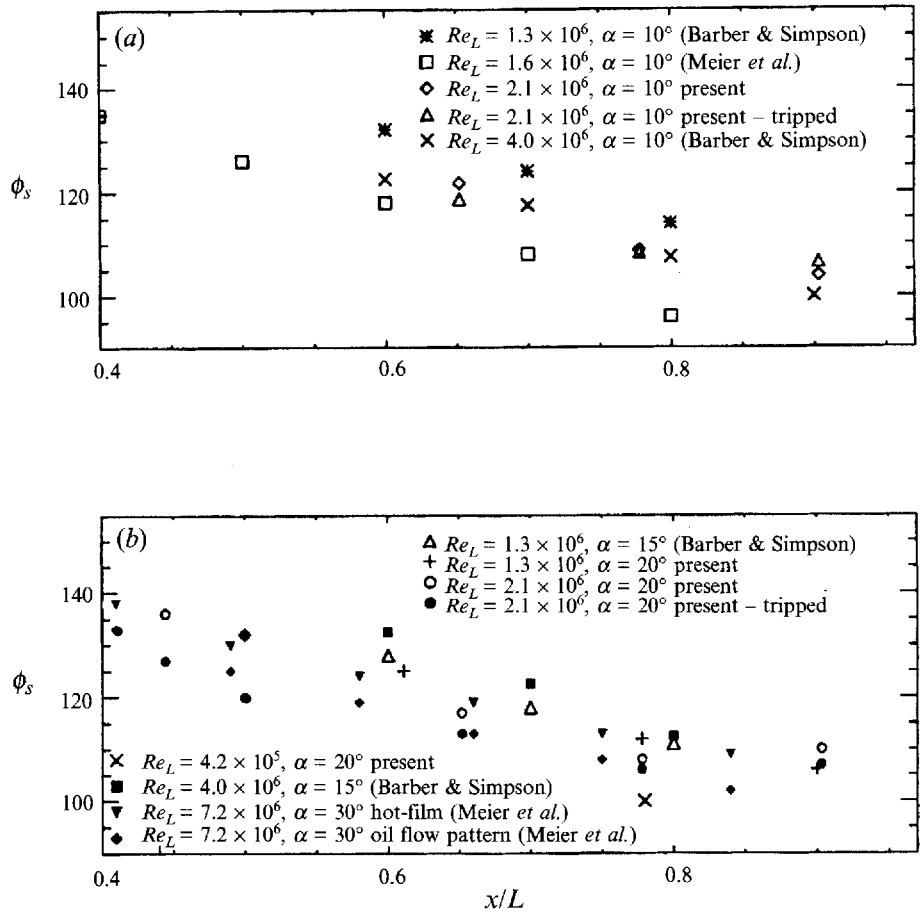

FIGURE 5. The location of boundary-layer separation.

and 'secondary' vortices is subjective and it is made based on their size and repeatability. Besides highlighting specific phenomena, these photographs are also used to demonstrate potential problems when PDV and auto-correlation analysis are utilized in regions with large velocity gradients. For example, figures 3(*b*) and 3(*e*) contain vector maps computed by utilizing 64 × 64 pixel windows while analysing the images shown in figures 3(*a*) and 3(*d*), respectively. The effect of averaging is particularly apparent in figure 3(*b*), since the characteristic lengthscales are smaller than the window size. To correct this problem the window size must be reduced, which is not always possible because of limitations in resolution and particle density. In places where the measurements could not be performed with a reduced widow size, the velocity was determined manually by correlating traces of individual particles. Sites with potential problems were identified by comparing velocity vectors in adjacent windows. The revised velocity maps are shown in figures 3(*c*) and 3(*f*).

3. Results

3.1. *Location of separation*

The location of separation on the body was determined by recording video images of light sheets oriented parallel to the direction of motion (axial sheets), and by

(*a*)

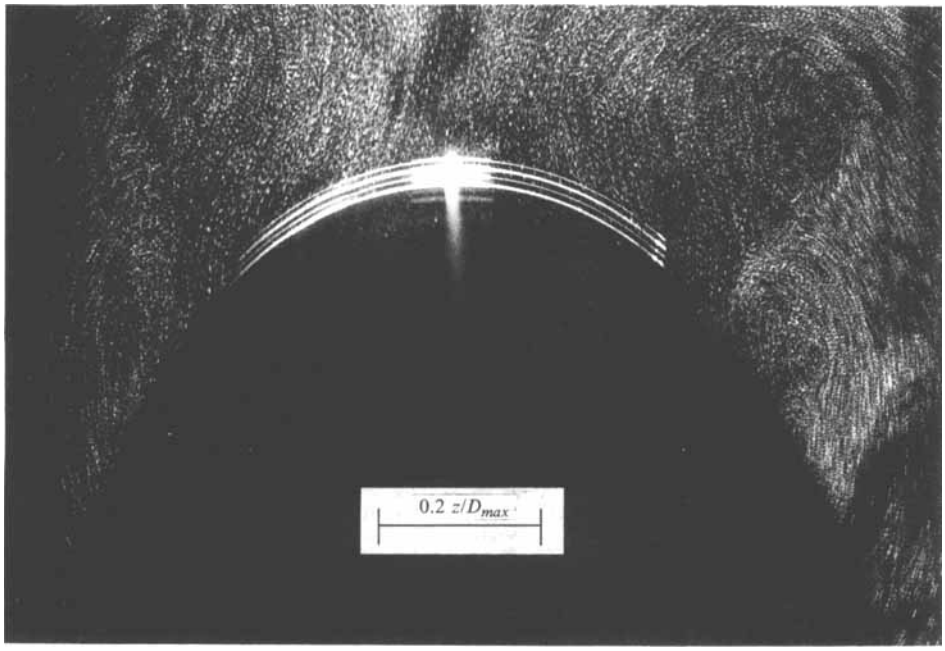

(*b*)

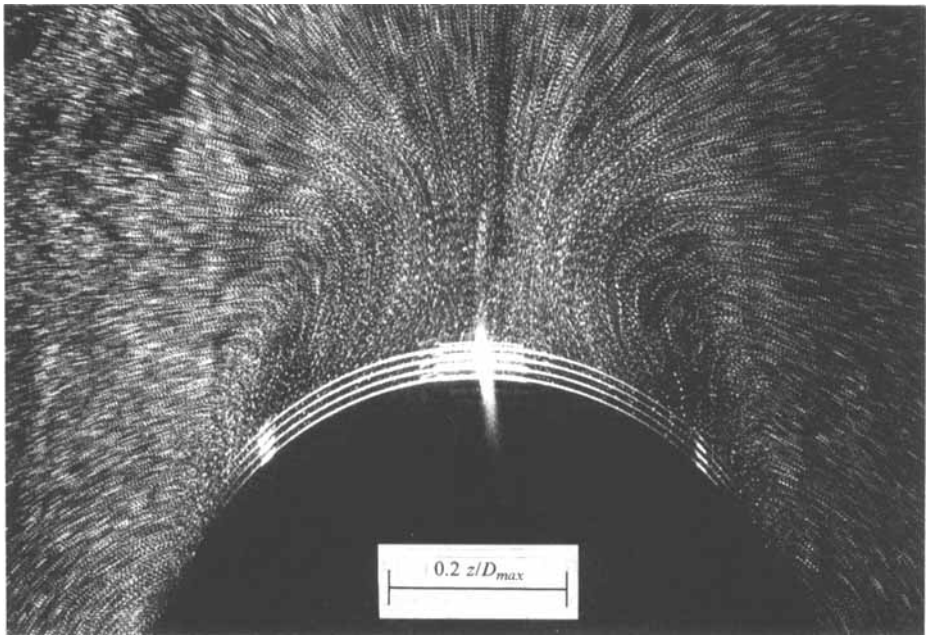

FIGURE 6. Images demonstrating Reynolds-number effects at $x/L = 0.78$ and $\alpha = 20°$: (*a*) $Re_L = 4.2 \times 10^5$; (*b*) $Re_L = 2.1 \times 10^6$.

distributing fluorescent dye in the water. A sample image of dye traces in the vicinity of the separation point is presented in figure 4. It demonstrates clearly the detachment of a limiting streamline from the surface of the body.

The location of boundary-layer separation is presented and compared to other

(*a*)

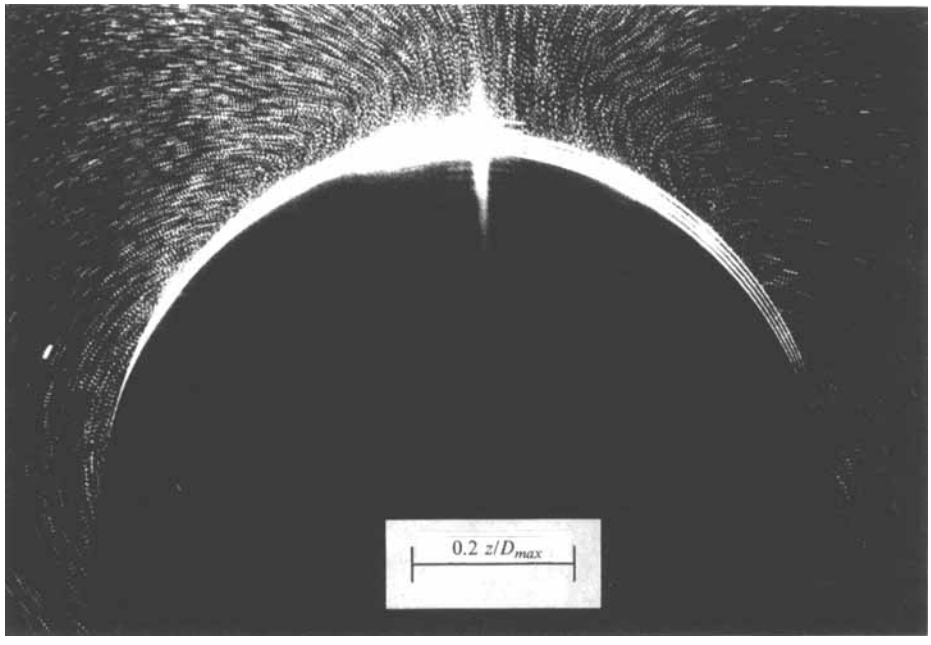

(*b*)

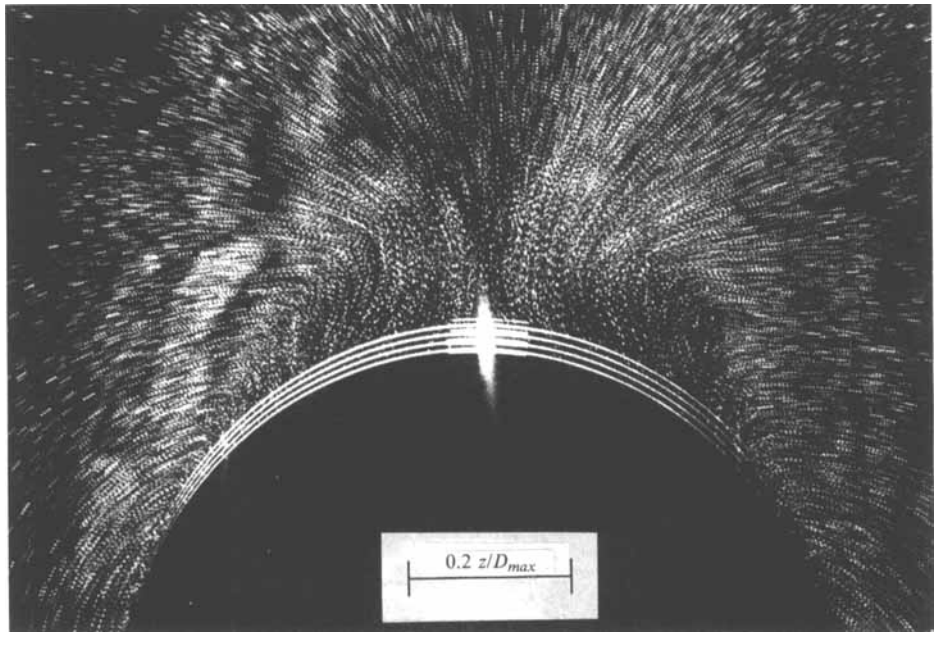

FIGURE 7. Images demonstrating axial variations in the flow structure at $\alpha = 20°$ and $Re_L = 2.1 \times 10^6$: (*a*) $x/L = 0.5$; (*b*) $x/L = 0.65$.

measurements in figures 5(*a*) and 5(*b*) (ϕ is the azimuthal angle, 0° being the windward meridian). At 10° incidence, the present separation line at $Re_L = 2.1 \times 10^6$ agrees with the results of Barber & Simpson (1990) at $Re_L = 4.0 \times 10^6$, but is considerably below (smaller ϕ) their data at $Re_L = 1.3 \times 10^6$. Tripping seems to have very little effect at

(*a*)

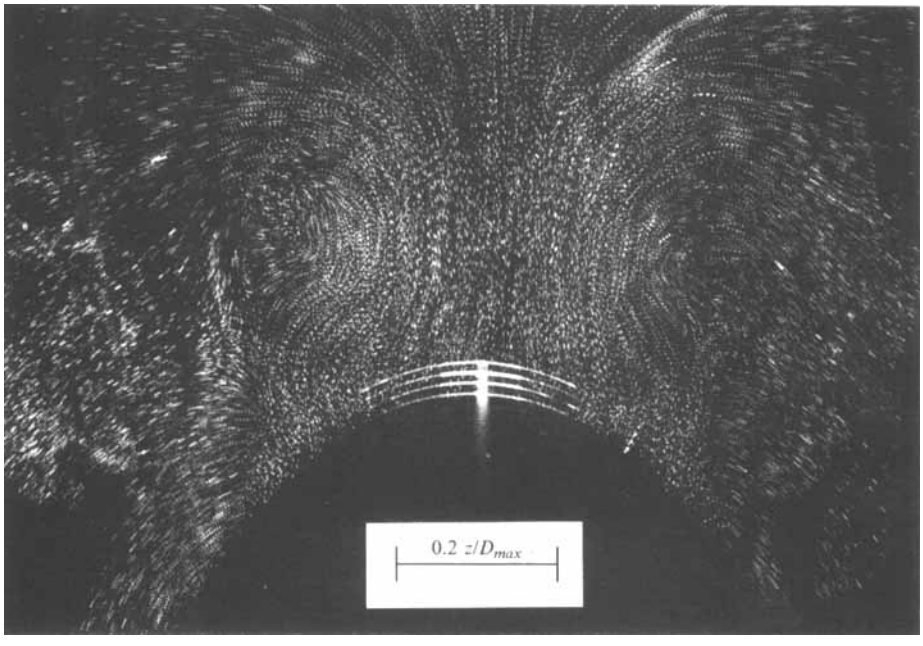

(*b*)

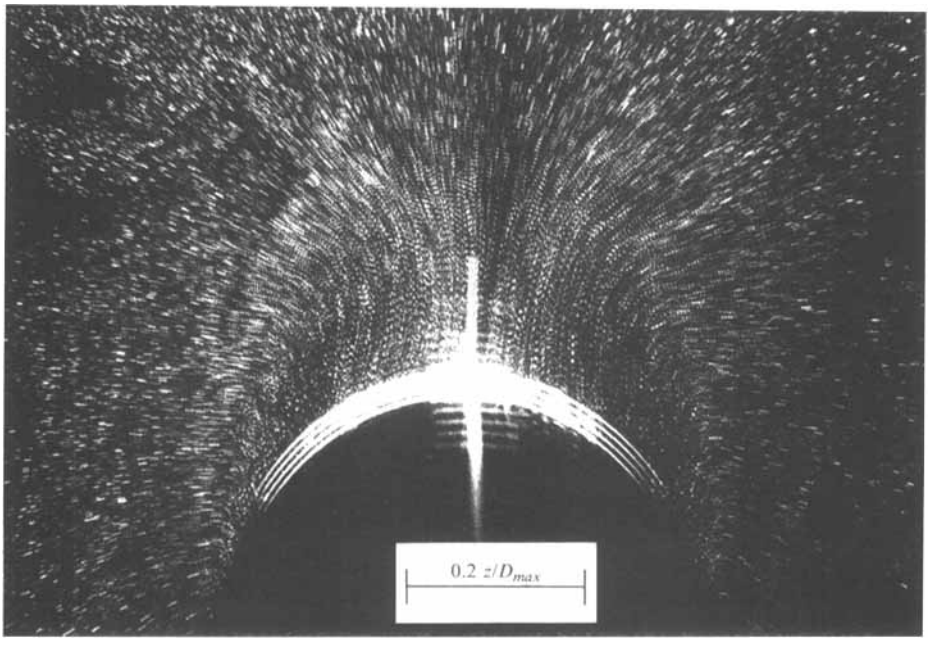

FIGURE 8. Incidence-angle effects on the flow structure at $x/L = 0.90$ and $Re_L = 2.1 \times 10^6$: (*a*) $\alpha = 20°$; (*b*) $a = 10°$.

such a low incidence. At 20° (figure 5*b*), tripping causes separation at a lower azimuthal angle up to $x/L \approx 0.7$, and has much less effect on the location of separation beyond this point. On a smooth body the separation point moves towards the leeward meridian as the Reynolds number is increased from 0.42×10^6 to 1.3×10^6. This trend is reversed

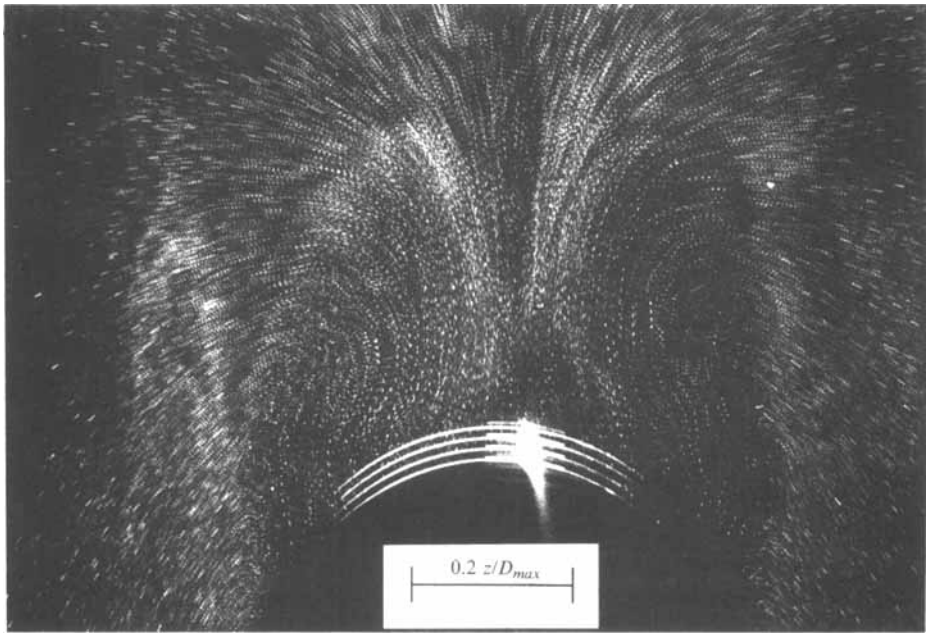

FIGURE 9. The flow structure when the boundary layer is tripped at $x/L = 0.90$, $Re_L = 2.1 \times 10^6$, and $\alpha = 20°$.

with further increase in Reynolds number of 2.1×10^6, namely the separation point moves slightly towards the windward meridian. This inconsistency probably occurs because the measurements are performed at Reynolds numbers in the transitional range. At 0.42×10^6 the boundary layer is predominantly laminar, and as the Reynolds number is increased the flow near the surface shows increasing signs of transition (increasing traces of secondary structures).

Since there is no other source of information on the location of separation at 20° incidence, the present measurements are compared to other experiments at 15° and 30°. At $Re_L = 1.3 \times 10^6$ the results fall slightly below the 15° data of Barber & Simpson (1990). Meier *et al.* (1983) provide two data sets at 30° incidence. The first set is measured with flush-mounted hot wires, and the second, with substantially earlier separation, is determined by surface oil visualization. They do not explain this discrepancy. The present results at 20° incidence are close to their hot-film data (at 30°) and above their surface-oil results. Since the present locations of separation fall between available data at 15° and 30°, one can at least conclude that the results are consistent.

3.2. *Qualitative observations*

Selected images aimed at demonstrating the characteristic flow structure in the lee of the model are presented in figures 6–9. The first (figure 6*a*) is a low-velocity ($Re_L = 4.2 \times 10^5$) image containing multiple secondary vortices. As the Reynolds number is increased, the presence of these secondary vortices becomes less evident, as shown in figure 6(*b*) (see also figure 2*a*). These structures do not disappear, as the vorticity distributions show (figure 11 for example), but their scale and form are such that it is hard to identify them from qualitative observations. Axial variations in the size and location of flow structures are presented in figure 7, while incidence angle effects can be observed by comparing figures 8(*a*) and 8(*b*). As expected, the dimensions of the

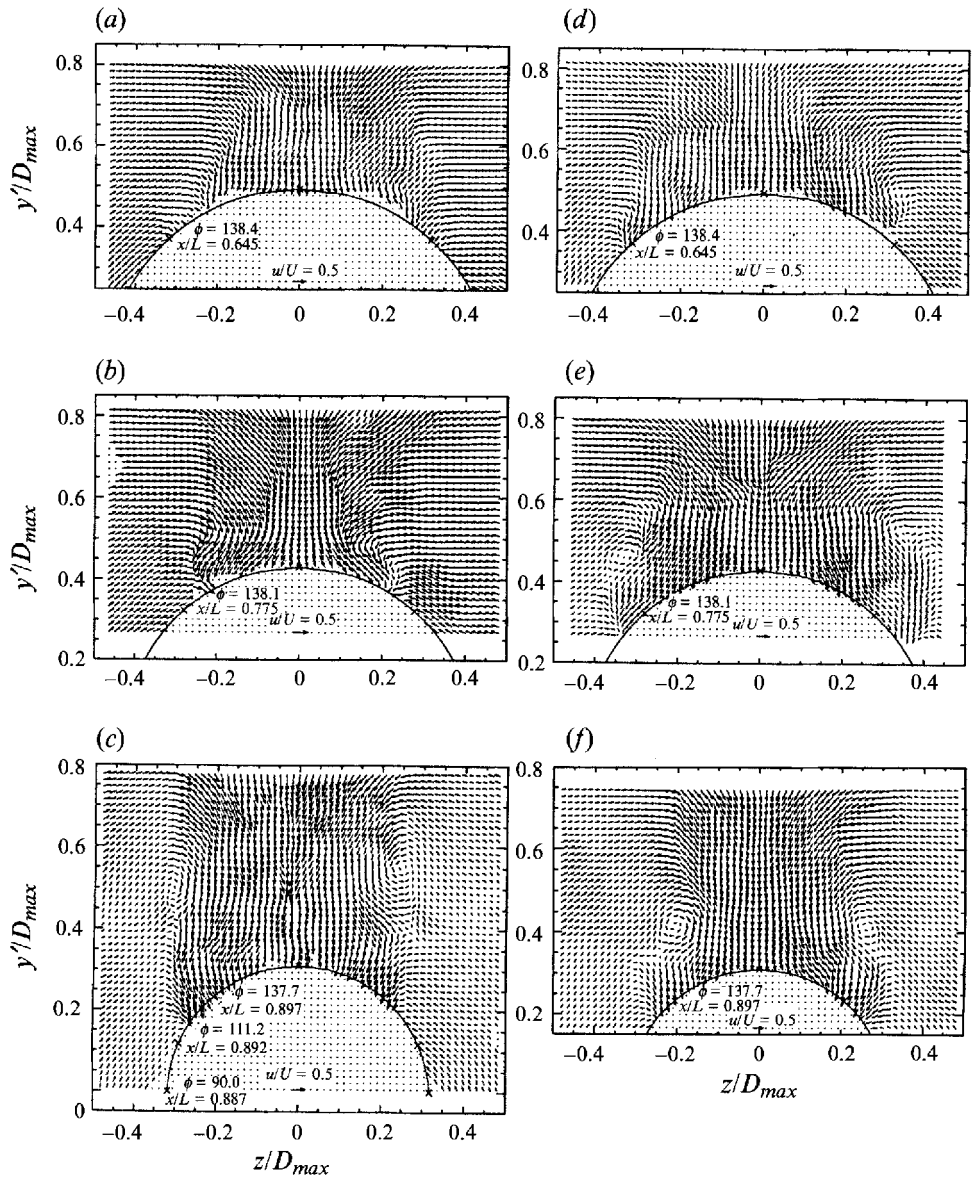

FIGURE 10. Instantaneous velocity distributions on: (*a–c*) a smooth body; (*d–f*) a body with a tripped boundary layer at $Re_L = 2.1 \times 10^6$, and $\alpha = 20°$. (*a*, *d*) $x/L = 0.65$; (*b*, *e*) $x/L = 0.78$; (*c*, *f*) $x/L = 0.90$. Note that observations are made from the front of the body.

region affected by boundary-layer separation increase with increasing x/L and increasing incidence angle. Finally, the effect of boundary-layer tripping is demonstrated by comparing figure 8(*a*) to figure 9. As a result of tripping, the secondary structures seem to disappear, and the primary vortices are located much closer to the surface. This qualitative assessment is only a clue to major changes in the velocity and vorticity distributions.

Surface flow visualization experiments performed by Wang *et al.* (1990) on a 4:1 sting-mounted prolate spheroid provided clear evidence that there was a reverse flow in the lee side at high x/L. Kim & Patel's (1991*a*) computations of the flow around a

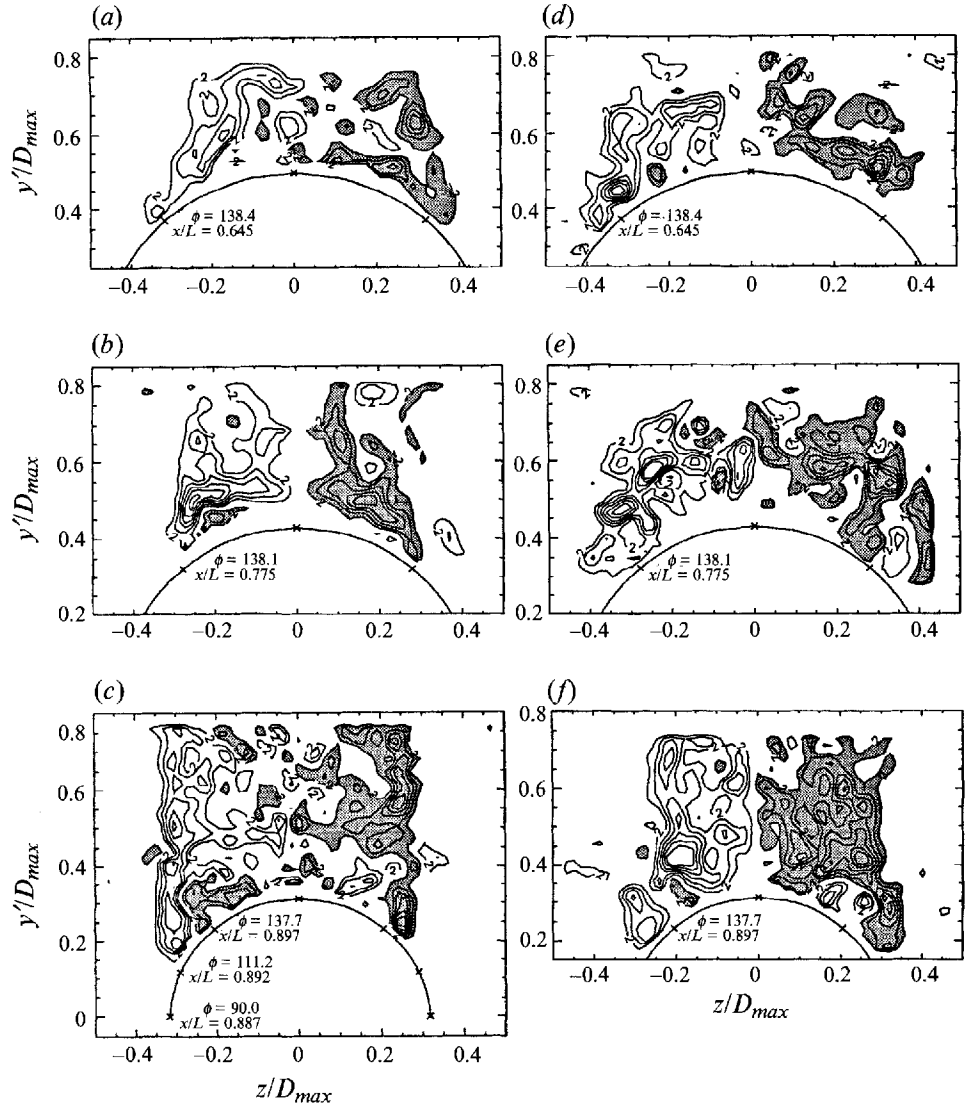

FIGURE 11. Instantaneous non-dimensional vorticity ($\omega_x D_{max}/U$) distributions computed from the data presented in figure 10. (*a*, *d*) $x/L = 0.65$; (*b*, *e*) $x/L = 0.78$; (*c*, *f*) $x/L = 0.90$. Grey areas denote negative vorticity. Incremental increase between lines is 2. Note that observations are made from the front of the body.

body with laminar separation, but without a sting, also demonstrated the same phenomenon. These observations led to careful examination of all of our available film and video records. There was no indication of a reverse flow on the lee side under any of the present test conditions. It is possible that the size of our sting (2 in. in diameter) and, to a lesser degree, the relatively high Reynolds number, prevented such a reverse flow. This argument is supported by Kim & Patel's (1991*b*) numerical results, in which a model with a sting and a turbulent boundary layer did not have any reverse flow.

3.3. *Velocity and vorticity distributions*

Selected instantaneous vector maps, illustrating axial variations in the flow structure, with and without boundary-layer tripping, are presented in figure 10. Note that the

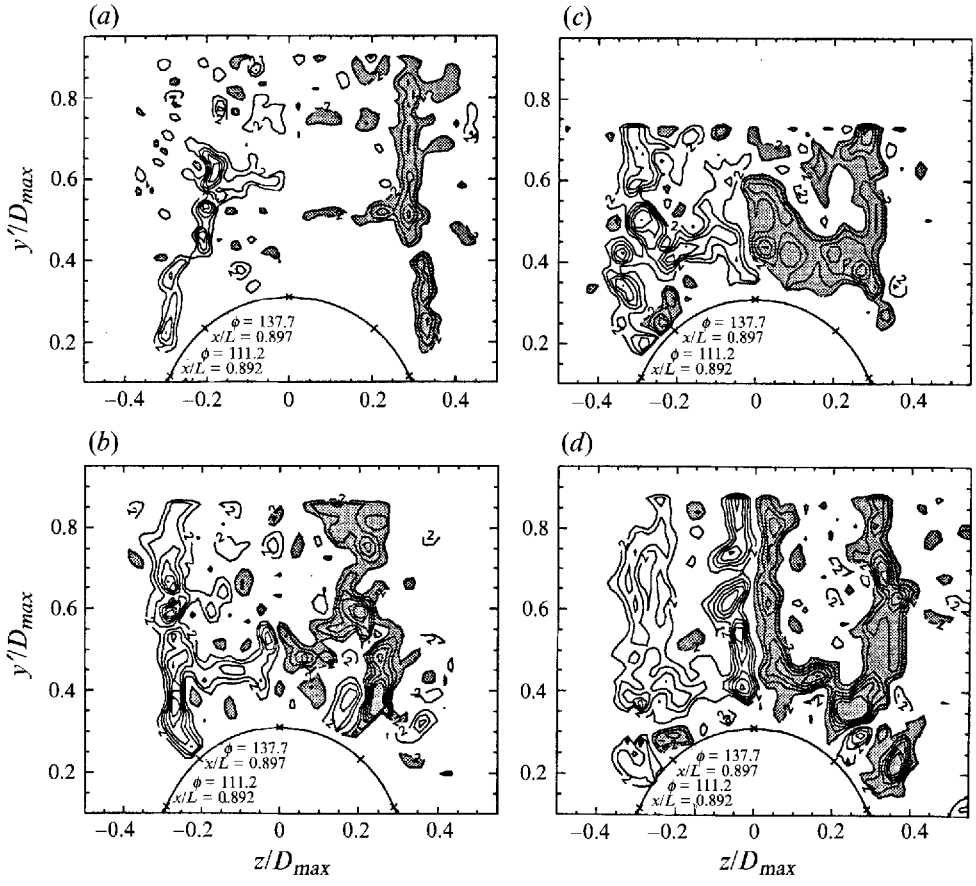

FIGURE 12. Instantaneous non-dimensional vorticity distributions (incremental increase of 2) on: (*a–c*) a smooth body; (*d*) a body with a tripped boundary layer, at $x/L = 0.90$, $Re_L = 2.1 \times 10^6$, and $\alpha = 20°$. Grey areas denote negative vorticity.

shape of the body cross-section is not circular owing to the orientation of the laser sheet. Consequently, values of ϕ and x/L are also indicated at several locations on each graph. The corresponding vorticity contour plots, determined by computing $\omega_x \approx \Delta w/\Delta y' - \Delta v/\Delta z$, where v and w are the velocity components in the y'- and z-directions, respectively, are presented in figure 11. The accuracy of the vorticity is only about 10%, since its computation involves a comparison between fairly close numbers. Several trends become evident from the results. First, in agreement with the previous qualitative observations, the region affected by flow separation (identified by the presence of rotational flow) increases with x/L only in the y'-direction, whereas the change in the z-direction is minimal. Second, boundary-layer tripping not only changes the location of the primary vortices, but it also alters the entire vorticity distribution. On the smooth body the vorticity seems to be concentrated within clearly defined regions, which at $x/L = 0.9$ resemble two symmetric vertical vorticity sheets with several discrete peaks. The highest peak, which is consistent with the location of the primary structure, has a dimensionless vorticity ($\omega_x D_{max}/U$) of about 6 at $x/L = 0.65$, and at least 10 at $x/L = 0.78$ and 0.9. The space between the sheets contains much less vorticity, and in some cases (see figure 12*a*), the flow is predominantly irrotational. These results indicate that the fluid located between the vorticity sheets does not pass

near the surface of the body, which allows it to remain vorticity free. This phenomenon can only happen if the region contains 'freshly' entrained external fluid, namely this zone cannot be part of an enclosed separated bubble. Thus, the flow in the lee side of the model under these conditions can be characterized as open separation.

On the tripped body the vorticity is distributed more uniformly over the entire lee side of the model. This trend should be expected since boundary-layer tripping causes a considerably higher level of turbulent diffusion (mixing), and as a result more uniformly distributed vorticity. At $x/L = 0.65$ there are still sites with irrotational flow, whereas further downstream, at $x/L = 0.78$ and 0.9, the vorticity is non-zero almost everywhere, and the contour plots contain several peaks with values ranging from $\omega_x D_{max}/U = 6$ to 8. The highest peaks (at $x/L = 0.78$ and 0.9), whose locations are consistent with the sites of the primary vortices (see the velocity distributions), are located much closer to the surface, but their magnitudes remain at the same levels as the smooth-body results. It seems that the increased level of turbulence, resulting from tripping, causes earlier rollup of a portion of the vorticity into distinct vortices. This dramatic change in flow structure has been consistently evident in all the data analysed during the present study. To the best of our knowledge, such a phenomenon has not been reported anywhere in the literature. However, as noted before, practically any experimental study performed with inclined bodies of revolution (Meier *et al.* 1983 and Han & Patel 1979, for example), showed sensitivity to the Reynolds number, presumably due to the characteristics of the boundary layer on the surface of the model.

Although not always obvious from the velocity maps, the presence of counter-rotating secondary vortex pairs near the surface is evident from the vorticity distribution. These structures exist even when the boundary layer is tripped, as shown for example in figure 11 (*f*). As noted before, Meier *et al.* (1983) could identify these vortices only at very low Reynolds numbers. The present results demonstrate that these structures exist even when the boundary layer is turbulent. Identification of these vortices with point measurement techniques is difficult because of meandering, the extent of which is discussed later. Note that these so-called 'secondary structures' are not always small, and the magnitudes of the vorticity peaks within them are comparable to those of the primary vortices. Since they are located closer to the surface, they may have a large impact on vibrations and unsteady forces acting on the body.

Additional vorticity plots, at the same conditions as the data in figures 11 (*c*) and 11 (*f*), are presented in figure 12 (*a*, *b*, *c* for a smooth body and *d* for a tripped body) to demonstrate the extent of variations between runs. It is clear that both the shape of the entire vortex sheets as well as the vorticity distributions within them vary substantially. In some cases all the vorticity is concentrated within the two vertical sheets (figure 12 *a*), whereas in others the distributions contain protrusions with varying sizes and strengths, that extend into the area between the main sheets. These extensions are weak in figures 11 (*c*) and 12 (*a*), but they have a considerable strength in figures 12 (*b*) and 12 (*c*). A similar phenomenon has been observed at other locations (figure 11 *b*, for example). In some cases, especially the tripped flow (figure 12 *d*, which is an extreme example) or low-Reynolds-number flows (figure 14), the inner extension is comparable, or even more powerful than, the 'main' vortex sheet. It is difficult to provide a substantiated explanation for this phenomenon, but we would like to propose one, as follows. It is clear from all the vector maps that the flow in the illuminated plane surrounds the vorticity sheets and then moves towards the surface of the body. In the process, this flow can either 'bend' or 'pinch' the upper portion (or most) of the vorticity sheet. It

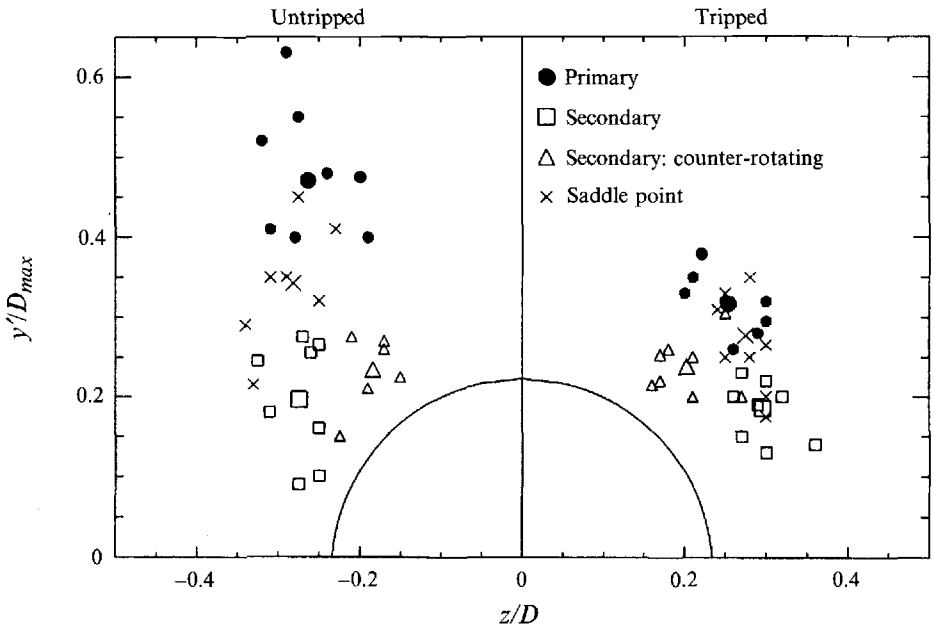

FIGURE 13. The location of foci and saddle points determined from several images at $x/L = 0.90$, $Re_L = 2.1 \times 10^6$, and $\alpha = 20°$, with (right side) and without (left side) boundary-layer tripping. Larger symbols indicate mean values.

then pushes the pinched portion towards the line of symmetry ($z = 0$), and convects it towards the surface. Owing to the high velocity in the middle, the pinched sections are most likely sheared off from the sheet, and appear as protrusions of various sizes and magnitudes within the predominantly irrotational region. In extreme cases, such as figure 12(*d*), almost the entire sheet is pushed at one time towards the centre. However, as the flow progresses downstream, the boundary layer keeps on feeding additional vorticity at the separation point, and creates what appears to be a second sheet. Since the entire vorticity distribution is modified, as the next section shows, there is a considerable effect on the overall forces on the body.

As is already evident by comparing figures 11(*c*), 12(*a*), 12(*b*) and 12(*c*), the entire vortex sheet and the main structures within seem to meander. This trend is also illustrated in figure 13, which compares the locations of singular points (foci, saddle points, and centres of secondary vortices near the surface) for smooth and tripped bodies. In spite of a considerable scatter in the results, it is still possible to recognize that boundary-layer tripping consistently shifts the location of the primary vortex and the saddle point below it closer to the surface. It is also clear that the extent of variability on a smooth body is higher. Probable causes include the transitional boundary layer, with associated higher intermittency, on the smooth body, and the earlier (lower y') rollup on a tripped body, which leaves less room for variability.

Figures 14 and 15 demonstrate Reynolds-number effects. Within the present range of measurements, the variability (instability) in flow structure is the highest at $Re_L = 4.2 \times 10^5$. This is evident from figures 14(*b*) and 14(*c*), which show two sample vorticity distributions measured under similar flow conditions. In each example the space between the 'primary' vorticity sheets contains major extensions with varying shapes and magnitudes. In the first distribution there are also signs that both sheets have been pushed towards the centreline at an earlier stage (lower x/L). The flow instability is

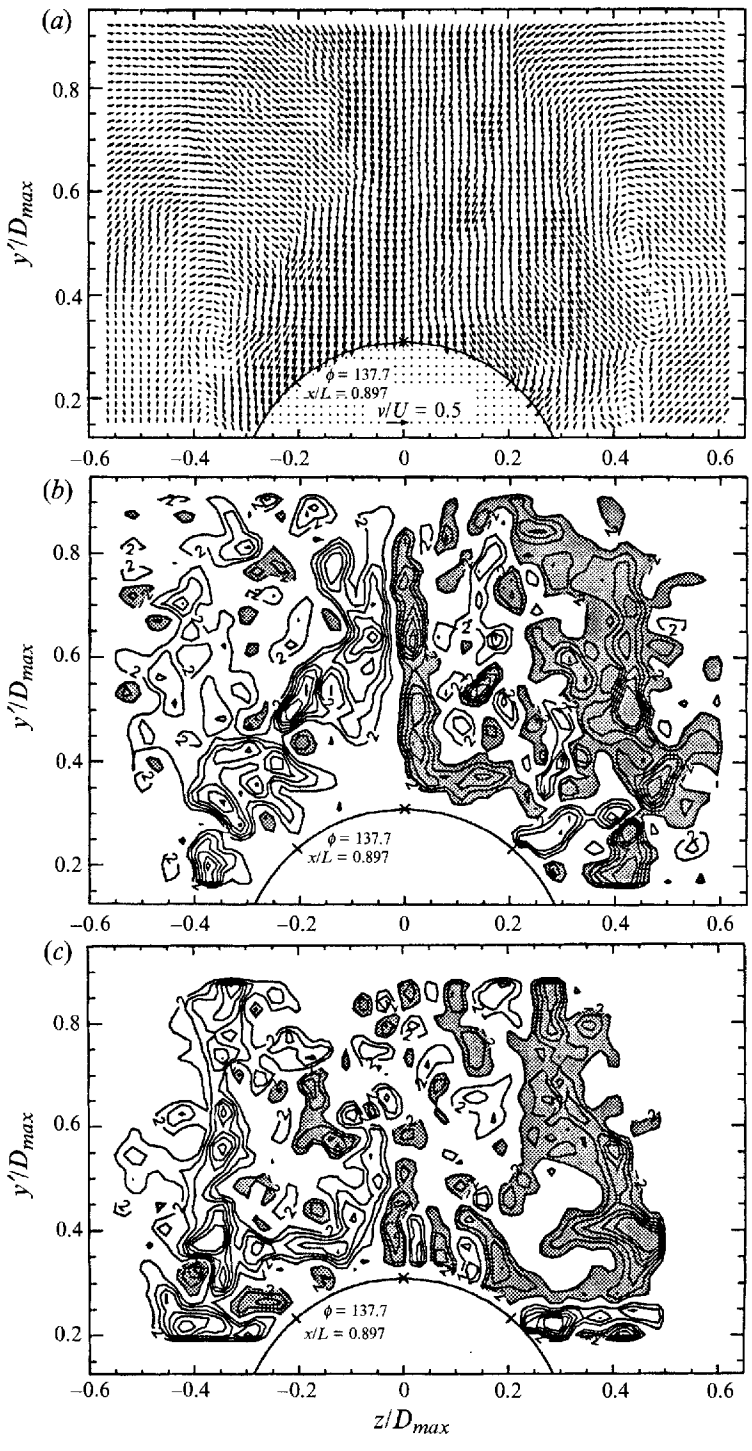

FIGURE 14. Characteristic (*a*) instantaneous velocity and (*b*, *c*) non-dimensional vorticity distributions (incremental increase of 2), at $Re_L = 4.2 \times 10^5$, $\alpha = 20°$, and $x/L = 0.90$. (*a*) and (*b*) represent the same image. Grey areas denote negative vorticity.

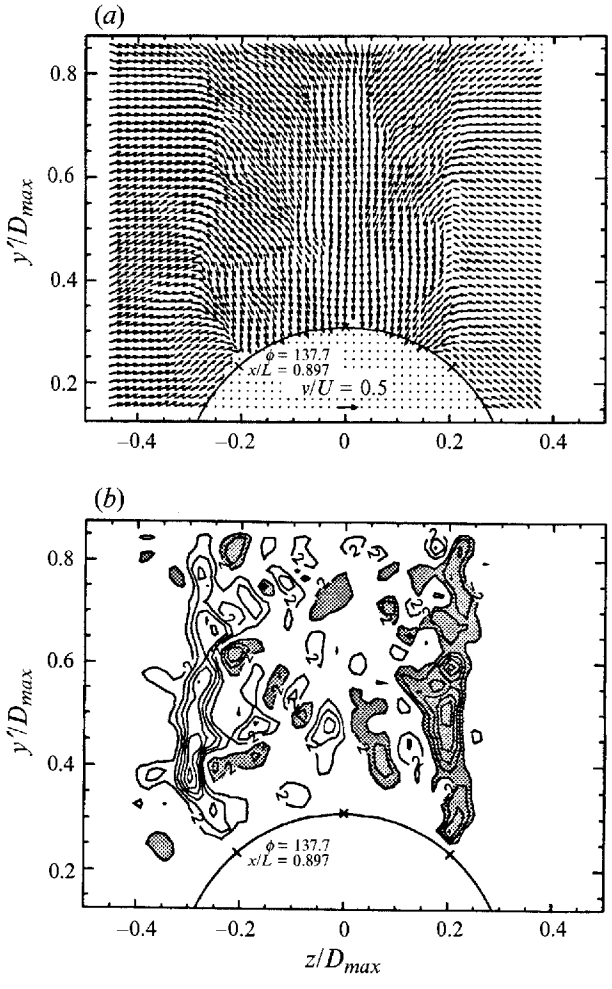

FIGURE 15. Characteristic (*a*) instantaneous velocity and (*b*) non-dimensional vorticity distributions (increment between lines is 2), at $Re_L = 1.3 \times 10^6$, $\alpha = 20°$, and $x/L = 0.90$. Grey areas denote negative vorticity.

also demonstrated by the presence of several distinct co-rotating vortices inside each vorticity sheet (see also figures 6*a* and 14*a*). The associated dimensionless vorticity peaks are comparable in magnitude and are as high as the primary vortex at $Re_L = 2.1 \times 10^6$. It is also evident from figure 14 that at $Re_L = 4.2 \times 10^5$ the primary sheets are located further away from the centreline, in agreement with the measured location of separation (figure 5). As the Reynolds number is increased to 1.3×10^6 (figure 15), the flow becomes more organized and the vorticity distribution resembles the results at $Re_L = 2.1 \times 10^6$ (figures 10–12), although the peaks are about 20% lower. Note that it is still difficult to identify the primary structure since the vorticity distributions contain several peaks with similar sizes and strengths.

Two sample velocity and vorticity distributions at 10° incidence are presented in figure 16 to demonstrate differences from the data at 20°. Here the size of the region with rotational flow is considerably smaller, with maximum values of less than half of those at 20°. The peak magnitudes are consistent with Barber & Simpson's (1990) hot-wire measurements. At $x/L = 0.78$ the vortex sheet appears to be wrapped around the

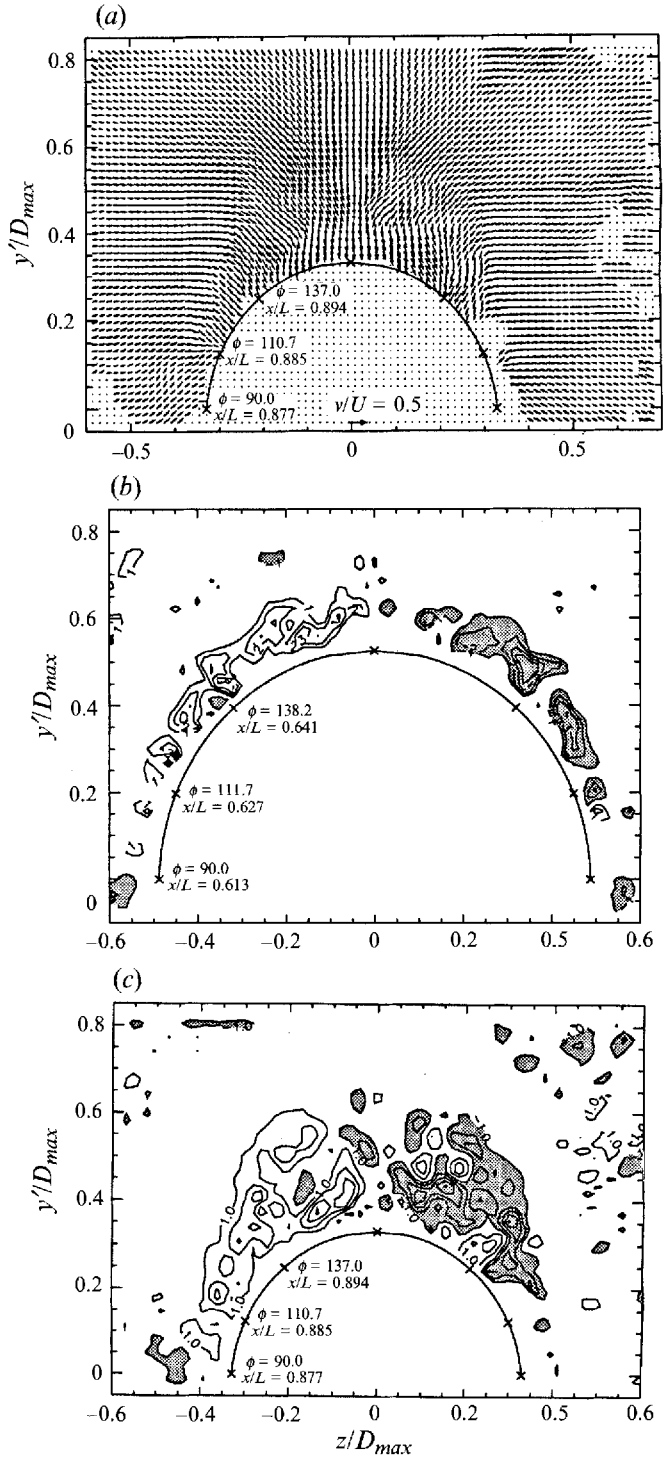

FIGURE 16. Characteristic (*a*) instantaneous velocity and (*b*, *c*) non-dimensional vorticity distributions (increment between lines is 1.0 and 1.5 for *b* and *c*, respectively), at $\alpha = 10°$ and $Re_L = 2.1 \times 10^6$. (*a*, *c*) $x/L = 0.90$; (*b*) $x/L = 0.65$. Grey areas denote negative vorticity.

body, and each side contains at least three centres, the largest of which is only slightly more powerful than the other two. At $x/L = 0.9$ the vortex sheet detaches from the surface and major vorticity peaks appear on each side of the body

4. Circulation, forces and moments

A qualitative description of the wake structure in the lee of the model, inferred from the PDV measurements, is presented in figure 17. It emphasizes the presence of the vorticity sheets, counter-rotating secondary structures, and that a considerable portion of the vorticity remains distributed outside of clearly defined vortices. In the following sections we discuss the implications of these results. First, the circulation, and how it is distributed within different parts of the wake are calculated. Then the vorticity distributions are used also for estimating the forces and moments on the body. The results compare favourably to available data on direct force measurements. Effects of tripping, Reynolds number and incidence angle are also discussed.

4.1. *Circulation*

The circulation can be computed either by integrating the vorticity over an appropriate section, or by line integration of the velocity component tangent to the contour enclosing this section. Since these methods use different data, a comparison between them is a measure of how well one can use the vorticity distributions for computing the circulation and forces (see the next section) on the body. Results of such a comparison, showing the overall circulation (Γ) over half of the body ($z < 0$ or $z > 0$), are presented in figure 18(*a*). It is evident that the difference between these methods is, for most cases, in the order of 2%, and can be considered to be insignificant. Distributions of Γ for several sections, presented in figures 18(*b*) and 18(*c*), display several trends. First, tripping increases the average circulation only in upstream sections ($x/L \leqslant 0.78$), but increases the variations between runs everywhere. Second, as one can also conclude easily from the vorticity distributions, the dimensionless circulation (Γ/UD_{max}) decreases as the Reynolds number is increased from 4.2×10^5 to 2.1×10^6. Third, an increase in incidence angle from 10° to 20° increases the circulation by 2.5–3 times. Thus, unlike most lifting surfaces, the circulation is not proportional to the incidence angle. Differences in the location of separation, which increase the effective 'lifting area' as the incidence angle is increased, can account for the discrepancy.

As figures 11, 12, 14, 15, and 16 show qualitatively, only a portion of the vorticity shed from the body is concentrated within distinct vortices. Computed percentages of the total circulation, obtained by integrating the vorticity within selected structures, are presented in figures 18(*d*) and 18(*e*). At $x/L = 0.65$ and 0.78, the primary vortex on a smooth body contains between 30% and 55% of Γ. At $x/d = 0.9$ there is some decrease to 20%–40%, but the difference is not sufficient for definite conclusions. Thus, entrainment of vorticity into the primary structure lags only slightly behind the rate at which Γ increases with x/L (figure 18*b*). The strengths of the so-called secondary vortices, which are located near the body, range between 10% and 25% of Γ. These fractions do not seem to vary with axial location. Between 40% and 75% of the circulation on a smooth body remains distributed outside of distinct vortices, either in the main vorticity sheets or in the protrusions into the central region. The latter contain between 20% and 40% of Γ. On the tripped body the strength of the primary vortex varies between 17% and 50% of Γ, a wider range than for the smooth body. There is no clear variation with x/L (although the mean percentage at $x/L = 0.9$ is lower). The secondary vortices near the surface vary between 5% and 25%, and the

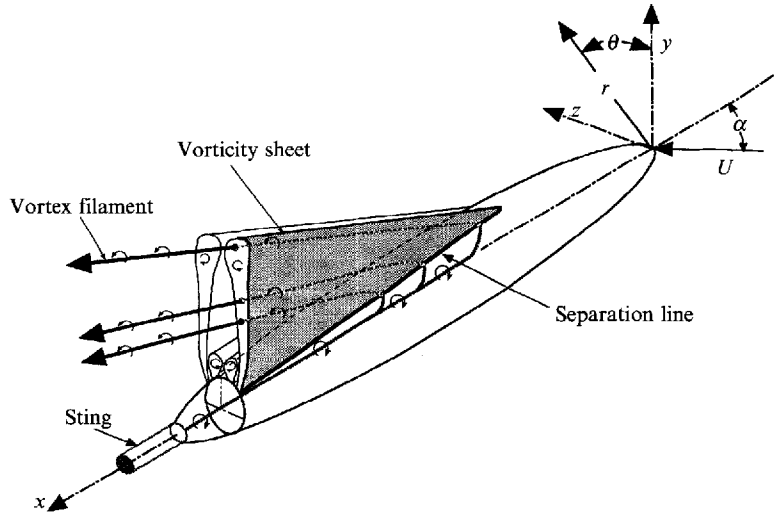

FIGURE 17. A sketch illustrating the trajectory of several vortex filaments shed from the body, and their corresponding 'images' within the model.

protrusions contain 20%–65% of the circulation. Between 40% and 80% of Γ remains outside of the vortices, similar to the smooth body. For both cases there is considerable variability in the location, spatial distribution and percentage of vorticity rolled up into distinct vortices. Although tripping changes the location of the vortices (figure 13), it does not have a clearly identified effect on their strength.

4.2. *Forces and moments*

The availability of detailed vorticity distributions enables direct determination of the lift and side forces on the body. The procedure uses classical theories on the relationship between the vorticity trailing behind a wing and the lift force, and has been used recently for estimating forces on wings using the results of point measurements (Ward & Wilson 1992 and Brune 1992, for example). Based on potential flow theory, every free vortex shed from a surface element of a body (figure 17) must be matched by an internal counter-rotating vortex. Their presence results, according to the Kutta–Joukowski theorem, in a force whose magnitude and direction in the cross-plane is

$$\mathrm{d}\boldsymbol{F} = \rho U r \omega_x r \,\mathrm{d}\theta \,\mathrm{d}r \boldsymbol{i}_\theta. \tag{1a}$$

Then, by integration, using the measured vorticity distribution, it is possible to determine the overall force. For example, if the y-component of $\mathrm{d}\boldsymbol{F}$ is $\rho U r \omega_x r \,\mathrm{d}\theta \,\mathrm{d}r \sin\theta$, then the overall force on the left-hand size ($Z < 0$) is

$$F_{YL} = \rho U \int_0^\infty \int_\pi^{2\pi} r \omega_x r \,\mathrm{d}\theta \,\mathrm{d}r \sin\theta. \tag{1b}$$

Coordinate transformation leads to the following results:

$$C_{YL} = \frac{F_{YL}}{\frac{1}{2}\rho U^2 L^2} = \frac{-2}{UL^2} \int_0^{-\infty} \int_{-\infty}^{\infty} z \omega_x \,\mathrm{d}y' \,\mathrm{d}z; \quad C_{YR} = \frac{F_{YR}}{\frac{1}{2}\rho U^2 L^2} = \frac{-2}{UL^2} \int_0^{\infty} \int_{-\infty}^{\infty} z \omega_x \,\mathrm{d}y' \,\mathrm{d}z, \tag{1c}$$

$$C_{ZL} = \frac{F_{ZL}}{\frac{1}{2}\rho U^2 L^2} = \frac{-2}{UL^2} \int_0^{-\infty} \int_{-\infty}^{\infty} y \omega_x \,\mathrm{d}y' \,\mathrm{d}z; \quad C_{ZR} = \frac{F_{ZR}}{\frac{1}{2}\rho U^2 L^2} = \frac{-2}{UL^2} \int_0^{\infty} \int_{-\infty}^{\infty} y \omega_x \,\mathrm{d}y' \,\mathrm{d}z, \tag{1d}$$

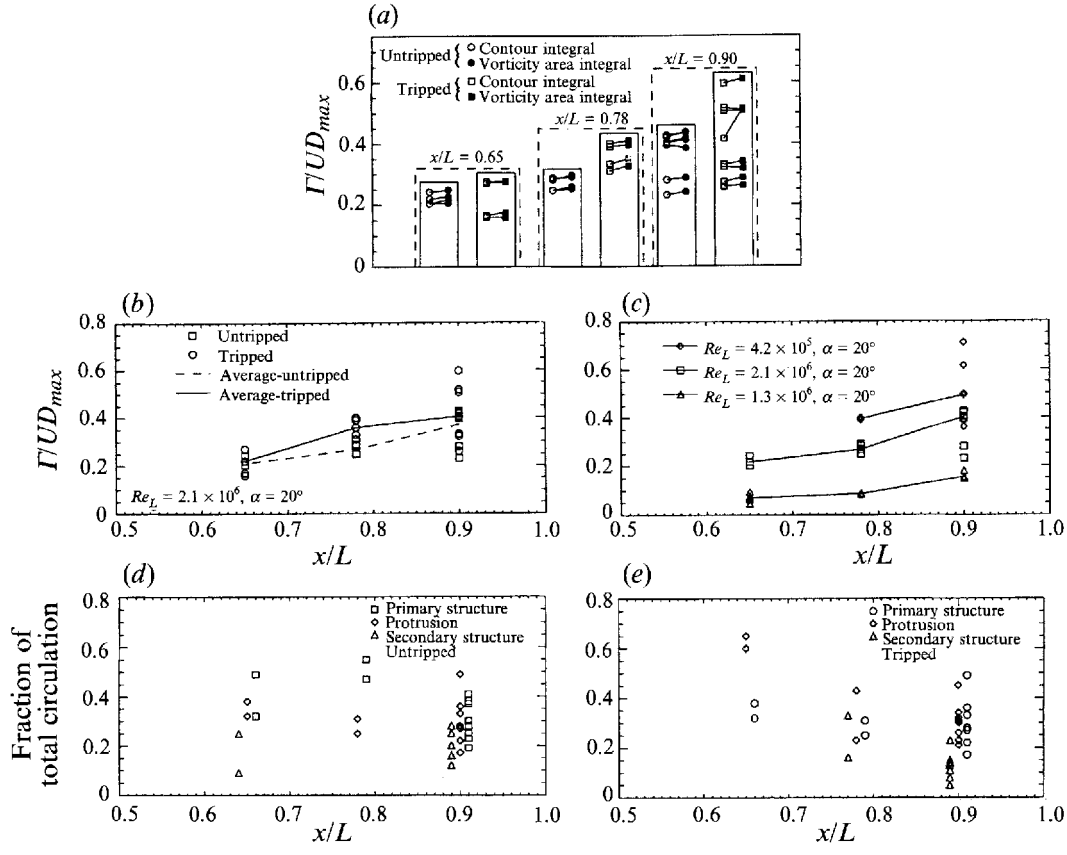

FIGURE 18. (*a*) A comparison between methods for computing the circulation; (*b*, *c*) axial distributions of circulation; (*d*, *e*) fraction of overall circulation enclosed within specific structures. Data are shifted slightly from their exact location ($x/L = 0.65$, 0.78 and 0.9) for clarity.

where F_Y and F_Z are the lift and side forces, respectively, C_Y and C_Z are corresponding force coefficients, and ρ is the fluid density. Since the instantaneous flow structure is asymmetric, the forces on each side of the model are determined separately, with subscripts L and R denoting left (negative z) and right sides (positive z), respectively. By calculating the moments, the same approach can be used to determine the location of action of the normal and side forces (Z_C, Y_C, respectively). The resulting equations are

$$Z_{C_{YR}} = \frac{-1}{C_{YR} UL^3} \int_0^\infty \int_{-\infty}^\infty z^2 \omega_x \, dy' \, dz, \quad Y_{C_{ZR}} = \frac{-1}{C_{ZR} UL^3} \int_0^\infty \int_{-\infty}^\infty y^2 \omega_x \, dy' \, dz. \quad (2)$$

Differences in the magnitude and location of action of the normal and side forces on each side of the model can be used to estimate the rolling moments. Note that proper use of these equations requires measurements behind the body. Otherwise, the portion of vorticity that is shed behind the cross-plane is not included, and the result underestimates the total force. Unfortunately, owing to the presence of the sting and the strut, the present measurements extend only up to $x/L = 0.9$. However, as the distributions in figure 18 show, the rate of increase in circulation at high x/L is slow. As a result, it is reasonable to assume that the unaccounted portion, which is shed at $x/L > 0.9$, does not make a major contribution to the overall forces.

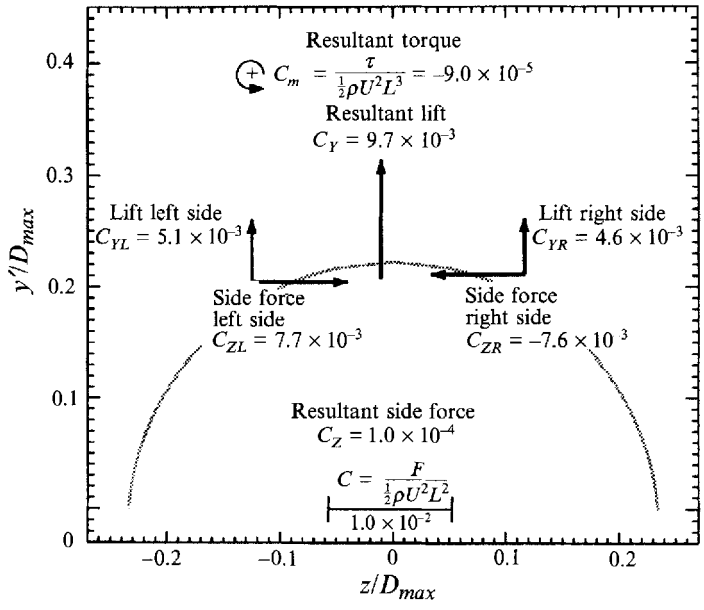

FIGURE 19. Instantaneous force and moment coefficients computed from the vorticity distribution presented in figure 12(*b*) ($x/L = 0.90$, $Re_L = 2.1 \times 10^6$, and $\alpha = 20°$).

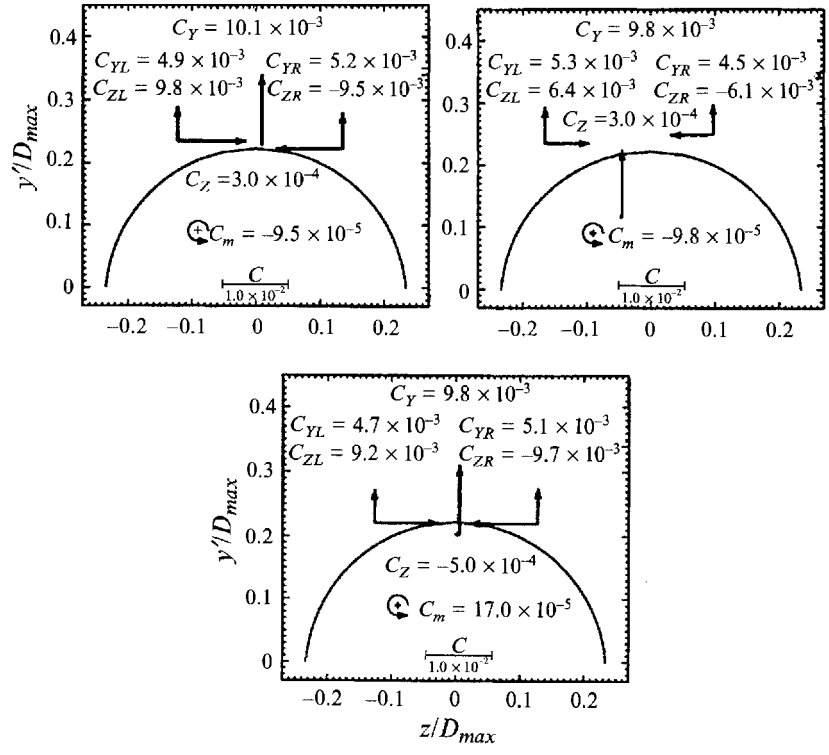

FIGURE 20. Instantaneous force and moment coefficients at $x/L = 0.90$, $Re_L = 2.1 \times 10^6$, and $\alpha = 20°$.

	Left side		Right side	
Trial no.	C_{YL}	C_{ZL}	C_{YR}	C_{ZR}
1	0.0023	0.0027	0.0018	−0.0027
2	0.0020	0.0023	0.0020	−0.0026

TABLE 1. Computed normal (C_Y) and side (C_Z) forces for the left (L) and right (R) sides of the model, at $Re_L = 2.1 \times 10^6$, $\alpha = 10°$, $x/L = 0.90$ and a smooth body. Method of calculation is defined in equation (1).

	$Re_L = 0.42 \times 10^6$				$Re_L = 1.3 \times 10^6$			
	Left side		Right side		Left side		Right side	
Trial no.	C_{YL}	C_{ZL}	C_{YR}	C_{ZR}	C_{YL}	C_{ZL}	C_{YR}	C_{ZR}
1	0.0097	0.0095	0.0083	−0.0093	0.0032	0.0034	0.0022	−0.0025
2	0.011	0.016	0.012	−0.015	—	—	—	—

TABLE 2. Sample computed normal and side forces at $\alpha = 20°$, $x/L = 0.90$ and a smooth body, for two Re_L values

A sample sketch of computed forces and their locations of action, as well as the overall rolling moment, using the data of figure 12(*b*), is presented in figure 19. Similar sketches demonstrating the variability in the instantaneous loads at the same conditions are presented in figure 20. Individual numerical results are presented in tables 1–4. Variations of the overall forces with x/L, and their dependence on incidence angle, Reynolds number, and boundary-layer tripping are presented in figures 21(*a*) and 21(*b*). Also included are results of previously unpublished force measurements performed at DTMB on inclined 6:1 prolate spheroids. The experiments were performed in a towing basin using a model supported by two struts. Force measurements were performed with two-component internal force balances, that were installed in each strut. The procedures (but not the prolate spheroid data) are described by Dempsey (1977). The agreement between the computed and measured forces is self-evident.

As the tables and figure 21 show, the mean values of C_Y increase from about 0.004 to 0.009 as the incidence angle is increased from 10° to 20°. Similar to the circulation (figure 19), the normal force is not proportional to the incidence angle. In both cases the present results at $Re_L = 2.1 \times 10^6$ are in good agreement with the direct measurements. As one would suspect from the vorticity distributions (figures 11, 12 and 14), there is also a substantial decrease in overall force coefficients as the Reynolds number is increased from 0.42×10^6 to 2.1×10^6.

Fluctuations in the overall forces and moments are significant. Based on the available data (it is recognized that this database is not sufficient for meaningful statistics), the r.m.s. fluctuation of the results on a smooth body are 6% for the normal force and 18% for the side force. Fluctuations in the locations of action of these forces are considerable ($\sim 30\%$), primarily due to meandering of the vortex sheet. These fluctuations cause considerable rolling moments, as shown in figures 19 and 20 and table 3(*b*).

Tripping seems to increase the r.m.s. fluctuations of C_Y and C_Z to about 34% and 32%, respectively. Since the force is dependent upon the spatial distribution of vorticity, one would expect to see such increased variability by examining the sample

	Untripped body				Tripped body			
	Left side		Right side		Left side		Right side	
Trial no.	C_{YL}	C_{ZL}	C_{YR}	C_{ZR}	C_{YL}	C_{ZL}	C_{YR}	C_{ZR}
1	0.0049	0.0098	0.0052	−0.0095	0.0052	0.012	0.0089	−0.013
2	0.0053	0.0064	0.0045	−0.0061	0.0035	0.0079	0.0041	−0.0075
3	0.0047	0.0092	0.0051	−0.0097	0.0046	0.011	0.0061	−0.011
4	0.0051	0.0077	0.0046	−0.0076	0.0037	0.0061	0.0043	−0.0052

TABLE 3. Computed normal and side forces, at $Re_L = 2.1 \times 10^6$, $\alpha = 20°$, and $x/L = 0.90$

	Untripped body					
	Left side		Right side		Overall	
Trial no.	Z_{CL}	Y_{CL}	Z_{CR}	Y_{CR}	C_M	C_Y
1	−0.020	0.039	0.023	0.037	-9.5×10^{-5}	0.0101
2	−0.027	0.039	0.016	0.041	-9.8×10^{-5}	0.0098
3	−0.021	0.037	0.021	0.037	1.7×10^{-4}	0.0098
4	−0.021	0.034	0.019	0.035	-9.0×10^{-5}	0.0097
	Tripped body					
	Left side		Right side		Overall	
Trial no.	Z_{CL}	Y_{CL}	Z_{CR}	Y_{CR}	C_M	C_Y
1	−0.021	0.038	0.026	0.036	9.5×10^{-4}	0.0141
2	−0.018	0.037	0.021	0.038	1.2×10^{-4}	0.0076
3	−0.017	0.036	0.021	0.035	2.4×10^{-4}	0.0106
4	−0.022	0.036	0.026	0.035	-4.9×10^{-5}	0.0080

TABLE 4. Dimensionless location of action of the normal and side forces, as well as overall normal force and rolling moment coefficient, corresponding to the data in table 3. The method of calculation is defined in equation (2).

distributions in figures 11 and 12. The variability in the size and location of vorticity protrusions into the central region as well as the large number of secondary structures are the primary contributors to these fluctuations. Note also that at $x/L = 0.78$ the mean force on a tripped body is a little higher, but the overall mean force, at least up to $x/L = 0.9$ does not change substantially. This trend is consistent with the circulation distributions shown in figure 18(*b*). The difference is probably a result of increased vorticity production when the boundary layer is turbulent. This difference seems to decrease close to the end of the body, in part since the untripped boundary layer also becomes turbulent.

5. Summary and conclusions

This paper presents results of detailed velocity measurements, using PDV, in the lee of an inclined body of revolution. They provide an insight into the flow structure and its dependence on Reynolds number (between 0.42×10^6 and 2.1×10^6), incidence angle (10° and 20°) and boundary-layer tripping. The vorticity distributions are used also for

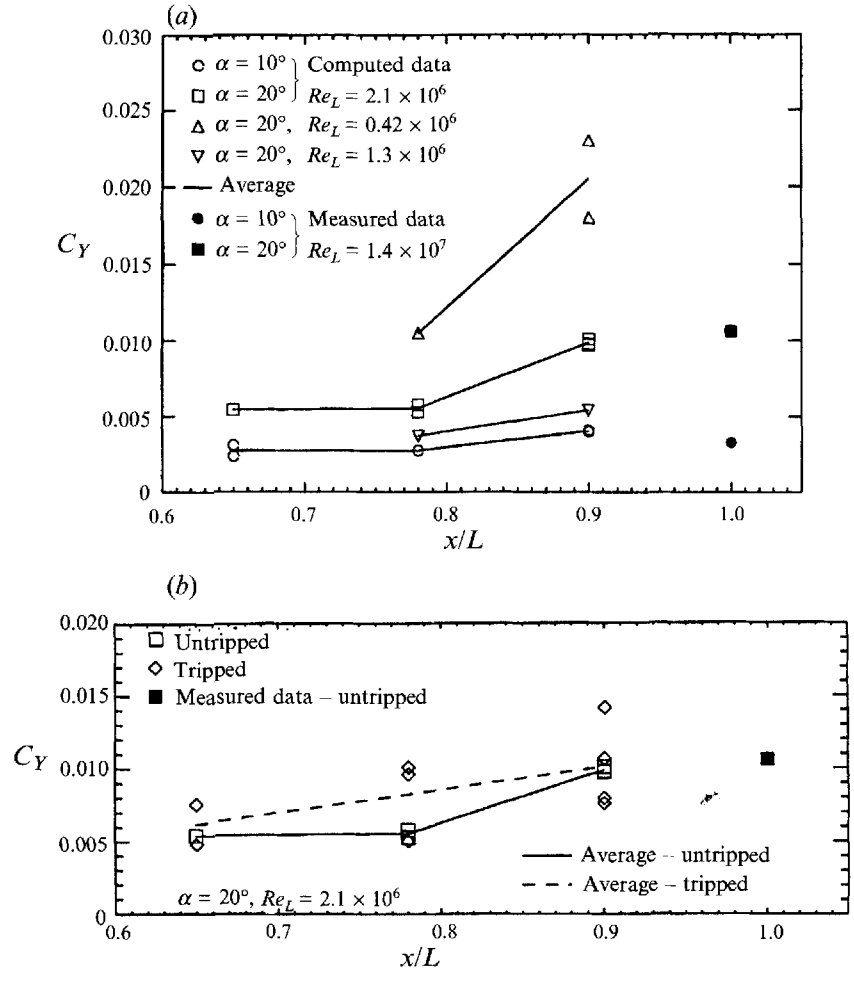

FIGURE 21. A comparison between computed and measured normal force coefficients.

estimating the forces and moments acting on the body. The conclusions of this study are as follows.

When the boundary layer is untripped, the flow separating from the surface creates a pair of vorticity sheets of opposite signs, on the lee side of the model. Portions of each sheet roll up into distinct vortices, the largest of which is referred to as the primary vortex. Its strength varies between 20% and 50% of the overall circulation. In some cases, however, the sheet contains several vorticity peaks with comparable sizes and magnitudes, and no peak is dominating. The overall size and circulation of these sheets, as well as the strength of distinct vortices within them, increase with axial location and incidence angle. The space between the vorticity sheets contains primarily irrotational flow. Hence the lee side flow can be characterized as open separation. The entire flow structure is quite unsteady, as the variability in location and shape of the sheets, as well as the number, position and strength of vortices located within them demonstrate. The vorticity distributions also contain isolated peaks and extensions, which are probably a result of 'pinching' or 'flip-flopping' of the sheet. As a result, the instantaneous flow structure can be quite asymmetric, causing considerable rolling moments. However, when averaged over time, the flow appears to be symmetric.

Pairs of counter-rotating 'secondary vortices' appear near the surface on both sides of the model. They have been seen before, but only at very low Reynolds numbers because of meandering. Their sizes and magnitudes also vary substantially, and in some cases are comparable to the 'primary vortices'.

Within the present range of test conditions the flow structure is sensitive to changes in Reynolds number, possibly as a result of boundary-layer transition. Compared to $Re_L = 2.1 \times 10^6$, the flow structure at $Re_L = 0.42 \times 10^6$ is more unstable, boundary-layer separation occurs at a lower azimuthal angle, and the vorticity sheets are located further away from the centreline of the model. Rollup of the vorticity sheets into a series of distinct vortices occurs more frequently and closer to the surface. The computed forces at $Re_L = 2.1 \times 10^6$ are in good agreement with direct measurements, and the forces at $Re_L = 0.42 \times 10^6$ are considerably higher.

Boundary-layer tripping at $Re_L = 2.1 \times 10^6$ spreads the vorticity over a wider area and increases the number of secondary structures, some of which appear to be distributed randomly. The scale and variability of vorticity protrusions into the central region also increase. Rollup of the vorticity sheets into distinct vortices occurs closer to the surface, but without significantly changing their size or magnitude. The increased variability causes high fluctuations in circulation and forces acting on the body, but the mean overall force remains almost unchanged.

This work was supported by the DARPA, Submarine Technology Program. The authors would like to thank Mr G. Jones, the area manager for his continued support. Thanks are also due to Ed Pogozelski for his assistance.

REFERENCES

BARBER, K. M. & SIMPSON, R. L. 1990 Mean velocity and turbulence measurements of flow around a 6:1 prolate spheroid. *VPI Rep.* VPI-AOE-174.

BRUNE, G. W. 1992 Quantitative three-dimensional low-speed wake surveys. In *Fifth Symp. on Numerical and Physical Aspects of Aerodynamic Flows, Cal. State Univ., Long Beach, Calif., Jan. 13–15* (ed. T. Cebici).

COSTIS, C. E., HOANG, N. T. & TELIONIS, D. P. 1989 Laminar separating flow over a prolate spheroid. *J. Aircraft* **86**, 810–816.

DEMPSEY, E. M. 1977 Static stability characteristics of a systematic series of stern control surfaces on a body of revolution, *David Taylor Naval Ship and Development Center, Rep.* 77-0085.

DONG, R., CHU, S. & KATZ, J. 1992*a* Quantitative visualization of the flow structure within the volute of a centrifugal pump, part A: Technique. *Trans. ASME* I: *J. Fluids Engng* **114**, 390–395.

DONG, R., CHU, S. & KATZ, J. 1992*b* Quantitative visualization of the flow structure within the volute of a centrifugal pump, part B: Results and analysis. *Trans. ASME* I: *J. Fluids Engng* **114**, 396–403.

GEE, K., CUMMINGS, R. M. & SCHIFF, L. B. 1992 Turbulence model effects on separated flow about a prolate spheroid. *AIAA J.* **30**, 655–664.

HAN, T. & PATEL, V. C. 1979 Flow separation on a spheroid at incidence. *J. Fluid Mech.* **92**, 643–657.

KIM, S. E. & PATEL, V. C. 1991*a* Laminar flow separation on a spheroid at incidence. *AIAA Paper* 91-1803.

KIM, S. E. & PATEL, V. C. 1991*b* Separation on a spheroid at incidence: turbulent flow. *Second Osaka Intl Colloqu. on Viscous Fluid Dynamics in Ship and Ocean Technology, Osaka, Japan, Sept. 27–30.*

MEIER, H. U. & KREPLIN, H. P. 1980 Experimental investigation of the boundary layer transition and separation on a body of revolution. *Z. Flugwiss. Weltraumforschung* **4**(2), 65–71.

MEIER, H. U., KREPLIN, H. P. & VOLLMERS, H. 1983 Development of boundary layers and

separation pattern on a body of revolution at incidence. In *2nd Symp. on Numerical and Physical Aspects of Aerodynamic Flows, State University, Long Beach CA, January* (ed. T. Cebici).

PEAKE, M. & TOBAK, D. J. 1982 Topology of three dimensional separated flow. *Ann. Rev. Fluid Mech.* **14**, 61–85.

SHEKARRIZ, A., FU, T. C., KATZ, J. & HUANG, T. T. 1993 Near field behavior of a tip vortex. *AIAA J.* **31**, 112–118.

SHEKARRIZ, A., FU, T. C., KATZ, J., LIU, H. L. & HUANG, T. T. 1992 Quantitative visualization of junction vortices using particle displacement velocimetry. *AIAA J.* **30**, 145–152.

WANG, K. C. 1972 Separation patterns of boundary layer over an inclined body of revolution. *AIAA J.* **10**, 1044–1050.

WANG, K. C. 1983 On the dispute about open separation. *AIAA Paper* 83-0296.

WANG, K. C., ZHOU, H. C., HU, C. H. & HARRINGTON, S. 1990 Three-dimensional separated flow structure over prolate spheroids. *Proc. R. Soc. Lond.* A **421**, 73–90.

WARD, K. C. & KATZ, J. 1989*a* Topology of the flow structures behind an inclined projectile: part A. *J. Aircraft* **26**, 1016–1022.

WARD, K. C. & KATZ, J. 1989*b* Topology of the flow structures behind an inclined projectile: part B. *J. Aircraft* **26**, 1023–1031.

WARD, B. & WILSON, P. A. 1992 Forces on a body of revolution in a vortex field. *The Royal Institution of Naval Architects, Paper* W4 (1992) (preprint).